

---

# KIC 9406652: A laboratory of the tilted disk in cataclysmic variable stars

Mariko KIMURA<sup>1,2,\*</sup>, Yoji OSAKI<sup>3</sup>, and Taichi KATO<sup>1</sup>

<sup>1</sup>Department of Astronomy, Graduate School of Science, Kyoto University, Oiwakecho, Kitashirakawa, Sakyo-ku, Kyoto 606-8502

<sup>2</sup>Extreme Natural Phenomena RIKEN Hakubi Research Team, Cluster for Pioneering Research, RIKEN, 2-1 Hirosawa, Wako, Saitama 351-0198

<sup>3</sup>Department of Astronomy, School of Science, University of Tokyo, Hongo, Tokyo 113-0033

\*E-mail: mariko.kimura@riken.jp

Received ; Accepted

## Abstract

KIC 9406652 is a cataclysmic variable, sub-classified as ‘IW And-type star’, showing a repetition of standstills with oscillatory variations terminated by brightening. This system showed negative superhumps, semi-periodic variations having periods slightly shorter than the  $\sim 6$ -hrs orbital period, and super-orbital signals having  $\sim 4$ -d periods, both of which are believed to originate from a precessing, tilted accretion disk. We have re-examined its *Kepler* light curve extending over 1500 d. In accordance with a cycle of the IW And-type light variation, the frequency of negative superhumps showed a reproducible variation: a rapid drop during the brightening and a gradual increase during the standstill. They are interpreted as the drastic change in the radial mass distribution and the expansion of the tilted disk, which is not expected from the existing models for IW And stars. The constancy in flux amplitudes of negative superhumps confirms that their light source is the bright spot sweeping across the surface of the tilted disk. The frequencies of negative superhumps and super-orbital signals varied in unison on long timescales, suggesting their common origin: the tilted disk. Orbital signals at the brightening were dominated by the irradiation of the secondary star and varied with the orientation of the tilted disk; the amplitude was maximized at the minimum of super-orbital signals and the light maximum shifted to early orbital phases as the super-orbital phase advances. This is the first direct evidence that the disk was tilted out of the binary orbital plane and retrogradely precessing. The tilt angle of the disk inferred from semi-amplitudes of super-orbital signals was lower than 3 degrees. The diversity in light curves of negative superhumps supports this and suggests that a part of the gas stream overflows the disk edge. This study thus offers rich information about the tilted disk in cataclysmic variables.

**Key words:** accretion, accretion disks - novae, cataclysmic variables - stars: dwarf novae - stars: individual (KIC 9406652)

---

## 1 Introduction

Cataclysmic variables (CVs), semi-detached close binary systems consisting of a white dwarf (WD) (the primary star) and a low-mass cool star (the secondary star), are a group of eruptive variable stars to which novae and dwarf novae belong. An

accretion disk is formed around the primary WD by the Roche-lobe overflow. The orbital period typically ranges from a few to several hours (Warner 1995 for a general review). Dwarf novae (DNe) show intermittent outbursts with a typical amplitude between 2–5 mag in the optical band with an interval of a

few weeks to hundred days and their outbursts are now believed to be caused by the thermal limit-cycle instability in the accretion disk (Osaki 1996 for a review on the disk instability). The thermal limit-cycle instability makes the accretion disk jump between the hot stable state and the cool stable state. When the system has the mass transfer rate ( $\dot{M}_{\text{tr}}$ ) from the secondary above the critical rate ( $\dot{M}_{\text{crit}}$ ), it persistently stays in the hot state, which is called a nova-like star (NL).

Z Cam-type DNe are known as an intermediate class between DNe and NLs, i.e.,  $\dot{M}_{\text{tr}} \sim \dot{M}_{\text{crit}}$ , in which the light curve alternates between DN outbursts and standstills on timescales of a few hundred days. The standstill is terminated by fading to the quiescent state in Z Cam stars. It has turned out that there exist a small number of unusual Z Cam stars (called ‘‘anomalous Z Cam Stars’’) (e.g., Simonsen 2011; Szkody et al. 2013; Simonsen et al. 2014) in which the standstill is terminated by brightening instead of fading. This brightening is sometimes called ‘a stunted outburst’ (e.g., Honeycutt 2001). Kato (2019) found three more such objects and recognized that they exhibit a characteristic light variation: a repetition of a quasi-standstill (i.e., a mid-brightness interval with (damping) oscillations) terminated by small brightening. He also named this class IW And-type DNe.

Two models have so far been proposed to explain the characteristic light variation in IW And-type DNe. The first one is proposed by Hameury and Lasota (2014) who argued the variation in the mass-transfer rate explains the brightening accompanied by a deep dip in IW And stars. The second model is proposed by Kimura et al. (2020) who studied the thermal-viscous instability in tilted accretion disks. The latter authors demonstrated that tilted disks can achieve a new kind of accretion cycle as mass supply patterns in the tilted disk are quite different from those in the usual non-tilted disk. In fact, the tilted disk is inferred in some IW And-type stars, since negative superhumps are detected in these stars (Armstrong et al. 2013; Gies et al. 2013).

Negative superhumps having periods shorter than the orbital period and super-orbital modulations having periods of a few to several days in CVs are believed to originate from the tilted accretion disk (e.g., Bonnet-Bidaud et al. 1985; Patterson 1999). The periodicity of negative superhumps is now considered to be produced by the beat period between the orbital period and the period with which the tilted disk retrogradely precesses and the light source is most likely variable dissipation in the bright spot which is produced by the collision of the gas stream with the disk matter, as the gas stream sweeps the disk surface with this period (Wood et al. 2000; Murray et al. 2002; Wood and Burke 2007). According to this interpretation, super-orbital modulations are naturally interpreted as the representation of the change in the projection area of the tilted disk against observers with the precession period. The implication of the tilted

disk in IW And-type stars motivated the authors of Kimura et al. (2020) to study the thermal-viscous instability in tilted disks, and hence, it becomes more important for us to know its detailed property. However, the property of the tilted disk in CVs has not so far been well investigated from observations.

A particular system, KIC 9406652, is interesting in this respect, because it exhibits typical IW And-type light variations and because good evidence of the tilted disk was already found in it (Gies et al. 2013). This system was observed by the *Kepler* satellite during  $\sim 4$  yrs. Gies et al. (2013) detected three kinds of periodic light variations, whose frequencies are 0.242, 3.929, and  $4.171 \text{ d}^{-1}$ , denoted as  $f_1$ ,  $f_2$ , and  $f_3$ , by using the *Kepler* data. They also performed spectroscopic observations and identified the orbital period to be 6.108-hrs which corresponds to  $f_2$ . They confirmed the relation of  $f_1 = f_3 - f_2$ , and hence, argued that  $f_1$  and  $f_3$  represent the frequency of the retrograde precession of the tilted disk and the frequency of negative superhumps originating from the bright spot on the tilted disk, respectively. Besides, they estimated the binary parameters of this system. The mass ratio and the inclination angle are determined to be  $0.83 \pm 0.07$  and  $\sim 50$  deg, respectively. Moreover, they estimated how the secondary and the disk contribute to the spectral energy distribution from ultraviolet to infrared wavelengths.

In this paper we re-investigate the *Kepler* data of KIC 9406652 to study the tilted disk in detail, just not only for IW And stars but also for CVs in general as its *Kepler* data have rich information. We aim to extend the existing study by Gies et al. (2013) and to extract as much information on the tilted disk as possible, by analyzing the time variations of frequencies, amplitudes, and light curve profiles of three periodic signals in detail. By so doing, we also examine the models for IW And-type stars so far proposed. This paper is structured as follows. Section 2 briefly describes the methods of the timing analyses. Section 3 presents our analyses of the *Kepler* light curves and their interpretations. In section 4, we discuss our results and examine the two models for the IW And-type stars and section 5 is the summary.

## 2 Methods of data analyses

### 2.1 Extraction of light curves

We have extracted the long-cadence *Kepler* public light curves. The long-cadence data integrate over multiple  $\sim 6$ -s exposures to give 1766-s observations and average short-lived events (Murphy 2012). We use the Simple Aperture Photometry (SAP) data. The count rates are converted to a relative magnitude by the formula  $\text{mag} = 14 - 2.5 \log e$  where  $e$  is the Kepler electron count rate ( $\text{electrons s}^{-1}$ ), and a constant of 14 is arbitrarily chosen for convenience. Hereafter we present all of the observation times in Barycentric Julian Date (BJD).

## 2.2 Period analyses

Before performing period analyses, we have subtracted the long-term trend of light curves from the observational data by locally-weighted polynomial regression (LOWESS: Cleveland 1979). We have to determine the length of the data for which we perform the regression and the smoother span influencing the smoothness of each data point in this method. When subtracting the trend of the overall light curve in subsections 3.2 and 3.3, we have performed LOWESS per 2 days with a smoother span of 0.4. On the other hand, we have divided the light curves into quasi-standstills and brightening, and have performed LOWESS for each data set to subtract the long-term trend in subsection 3.4. Then the smoother span ranged between 0.05–0.5 according to the light variation of each data set.

We have used the phase dispersion minimization (PDM) method (Stellingwerf 1978) for period analyses. The  $1-\sigma$  errors of PDM are calculated by the methods described in Fernie (1989) and Kato et al. (2010). A variety of bootstraps are applied to evaluate the robustness of the PDM result. We have prepared 100 samples, each of which randomly includes half of the observations, and performed the PDM analyses for the samples. The result of the bootstrap is displayed in the form of 90% confidence intervals in the resultant statistics.

In extracting the  $O - C$  curve of times of maxima and the full-amplitude variation of periodic modulations in subsections 3.2 and 3.4, we have derived the phase-averaged profile from a part of the observational data and have fitted each hump by using the profile as the template. The parameters to be obtained in that fitting for each hump are the time of the light maximum, from which the  $O - C$  is derived, the full-amplitude, and the offset of the brightness. Here  $O - C$  is defined as the times of maxima minus the constant period multiplied by the cycle of each hump and stands for the time derivative of periodic variations. The details of the method are described in Kato et al. (2009).

## 3 Results

### 3.1 Overall light curve

The overall *Kepler* light curve of KIC 9406652 is exhibited in the top panel of Figure 1. This light curve contains additional data of the Kepler observation quarter 16 (after BJD 2456392) in comparison with the data reported by Gies et al. (2013). This system shows very clearly the IW And-type phenomenon with a cyclic light variation as the quasi-standstill is terminated by brightening. Deep dips occasionally occur soon after brightening, though one exception was observed around BJD 2455190. Hereafter one cycle of the IW And-type phenomenon is defined as that from one brightening to the next, and we set the start as that from one brightening to the next, and we set the start as the beginning of brightening and its end as that of the next brightening. We display the borders of each cycle as dashed

lines in the top panel of Figure 1. The cycle length ranges from 30 to 110 d with its average value around 50 d and the amplitudes of brightening are less than but close to 1 mag. The Kepler data of this system extend over 1500 d and we identify 28 cycles as shown in the top panel of Figure 1. We find three types of periodic light variations: negative superhumps, orbital signals, and sometimes remarkable modulations with a  $\sim 4$ -d period called the super-orbital period, as reported by Gies et al. (2013). We study these three periodic signals in the following subsections.

### 3.2 Negative superhumps

#### 3.2.1 Correlation with the overall light variations

We first discuss negative superhumps (NSHs) as they are the most conspicuous sign of the tilted disk in CVs. The second, third, bottom panels of Figure 1 show the time evolution of the amplitude of negative superhumps in the magnitude scale, that in the flux scale, and of their frequency variation, respectively. Negative superhumps were clearly detected around BJD 2455300–2456300, and thus the disk is regarded to have been tilted in this interval. The amplitude of negative superhumps was very small and/or the hump shape was unclear before and after this interval, so that we were not able to explore the time variation of their frequencies and amplitudes. The IW And-type phenomenon appeared even when negative superhumps were very weak and/or non-existent. This may imply that the IW And-type phenomenon could occur regardless of whether the disk is tilted or not. The anomalous light variations such as a deep dip around BJD 2455190 and long-lasting brightening around BJD 2455230–2455290 (cycle 6) were observed just before negative superhumps clearly appeared. It is not known why this phenomenon occurred and whether or not it was related in any way to the development of negative superhumps.

#### 3.2.2 Frequency variations

The frequency variation of negative superhumps has information about the variation of the radius and the radial mass distribution of the tilted disk, as discussed in subsection 4.1. In this paper, we assume that the disk is rigidly tilted and does not have any warped structures. The frequency of the nodal precession of the rigidly tilted disk,  $\nu_{\text{nPR}}$ , is expressed as (Papaloizou and Terquem 1995; Larwood 1998):

$$\nu_{\text{nPR}} = -\frac{3}{8\pi} \frac{GM_2}{a^3} \frac{\int \Sigma r^3 dr}{\int \Sigma \Omega r^3 dr} \cos \theta, \quad (1)$$

where  $M_2$  is the mass of the secondary,  $r$  is the radial distance from the central WD,  $a$  is the binary separation,  $G$  is the gravitational constant,  $\Sigma$  is the surface density of the disk,  $\Omega$  is the Keplerian angular velocity of the disk matter, and  $\theta$  is the tilt angle, respectively. The minus sign in this equation means that the nodal precession is retrograde. The frequency of negative

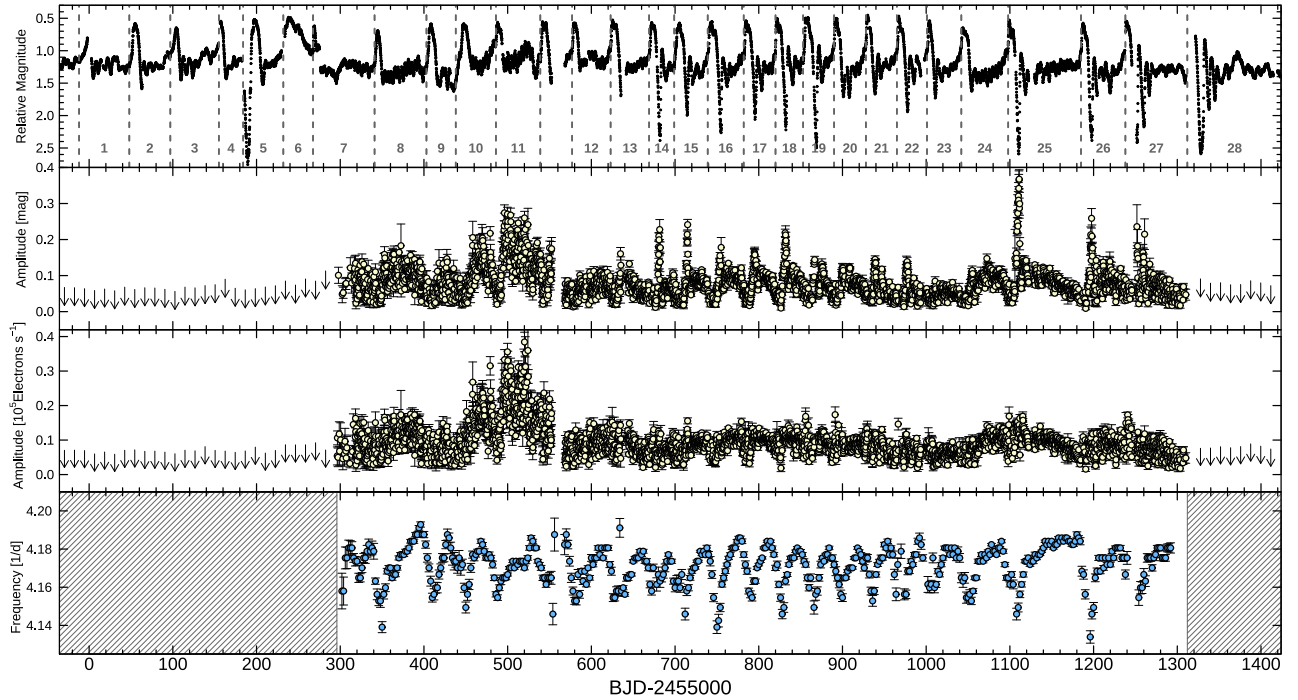


**Fig. 1.** Overall light curve, frequency variation, and amplitude variation of negative superhumps in KIC 9406652 during BJD 2454960–2456430. The first, second, third, and bottom panels represent the overall light curve, which is binned per 0.1 d, the amplitude in the magnitude scale, the amplitude in the flux scale, and the frequency, respectively. Each cycle of the IW And-type phenomenon is indicated by dashed lines in the top panel. The arrows in the second and third panels stand for the upper limit of amplitudes.

superhumps,  $\nu_{\text{NSH}}$ , is given by the synodic frequency between the tilted disk and the orbiting secondary star, and it is therefore expressed as

$$\begin{aligned} \nu_{\text{NSH}} = \nu_{\text{orb}} - \nu_{\text{nPR}} &= \nu_{\text{orb}} + \frac{3}{8\pi} \frac{GM_2}{a^3} \frac{\int \Sigma r^3 dr}{\int \Sigma \Omega r^3 dr} \cos \theta \quad (2) \\ &= \nu_{\text{orb}} + \frac{3}{8\pi} \frac{\sqrt{GM_2}}{a^3 \sqrt{M_1}} \frac{\int \Sigma r^3 dr}{\int \Sigma r^{3/2} dr} \cos \theta. \end{aligned}$$

Here  $\nu_{\text{orb}}$  is the orbital frequency of the binary and we use  $\Omega \equiv \sqrt{GM_1/r^3}$ , where  $M_1$  stands for the WD mass. We can safely put  $\cos \theta \simeq 1$  in equation (2) because the tilt angle in KIC 9406652 was found to be very small, almost always less than 3 deg in subsection 3.4.3. We, therefore, interpret that the frequency variation in KIC 9406652 would represent the time variation of the radial mass distribution and/or the radius of the tilted disk. Here we express the frequencies in two different ways in this paper,  $\nu$ , and  $f$ , where the former expression ( $\nu$ ) is that of physical origin and it can take a negative value while the latter one ( $f$ ) is the observed frequency of a periodic signal and it must be always positive. The three frequencies observed by Gies et al. (2013) correspond to  $f_1 = |\nu_{\text{nPR}}|$ ,  $f_2 = \nu_{\text{orb}}$ , and  $f_3 = \nu_{\text{NSH}}$ , respectively.

Let us now go back to observations. We first subtract the superimposed orbital signal with a period of 0.2545 d reported by Gies et al. (2013) to remove resonance signals. To extract the

frequency variation of negative superhumps, we apply PDM in a small window and repeated it by shifting the window by a certain time step (see also subsection 2.2). The width of the window is 12 d and the time step is 2 d, respectively. We also divide the interval between BJD 2455296 and BJD 2456312 into 6 short intervals and derive the  $O-C$  curve and the amplitude, since the  $O-C$  analysis is sensitive to the change of the hump shape. The resultant times of maxima of negative superhumps are given in Tables E1–E6 in the supplementary information.

The frequency variation takes a regular pattern every cycle of IW And-type phenomenon (see the bottom panel of Figure 1), that is, a sudden decrease in frequency by  $\sim 0.04\text{-d}^{-1}$  around the initial stage of brightening, which is sometimes accompanied with a small and rapid increase, and the gradual increase during the quasi-standstill. Although the start of decreases seems to sometimes precede the rapid rise of the luminosity in Figure 1, it is simply due to the artifact of our data analyses with the 12-d window width as discussed by Osaki and Kato (2013); Osaki and Kato (2014).<sup>1</sup> To show the period change more clearly, we pick up the time interval during BJD 2455720–2455865 and exhibit the results in an expanded form together with the  $O-C$  curve in Figure 2. The  $O-C$  curve clearly shows the sudden period increase at the beginning of brightening, which corre-

<sup>1</sup> We confirmed that the frequencies jumped in the almost same way in analyzing the same data with the 8-d window width.

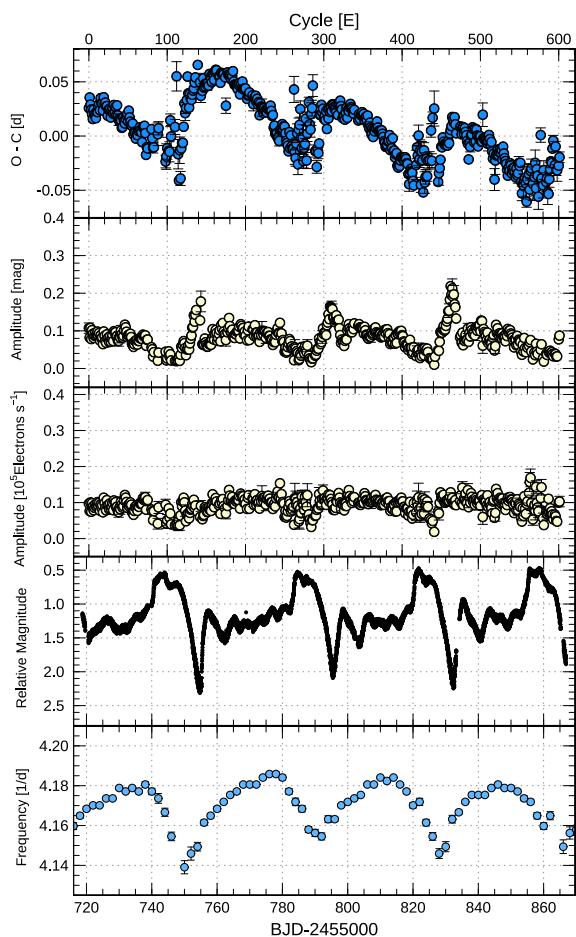


**Fig. 2.**  $O - C$  curve, amplitude variation, light curve, and frequency variation of negative superhumps in KIC 9406652 during BJD 2455720–2455865. Here, we use  $C = 2455720.7393 + 0.23988 E$ . The upper three panels are plotted against the cycle number  $E$  and the lower two panels are plotted against BJD, respectively.

sponds to the rapid decrease in the frequency. The interpretation of the time evolution of the frequency of negative superhumps will be discussed in subsection 4.1 concerning the modeling of the IW And-type phenomenon.

### 3.2.3 Amplitude and profile variations

The amplitude variation in the magnitude scale is displayed in the second panels of Figures 1 and 2 during one cycle of the IW And-type phenomenon. The upper limit of amplitudes are estimated by folding the 12-d light curves with a period of 0.2401 d before BJD 2455296 and with 0.2397 d after BJD 2456312. The pattern of amplitude variations in the magnitude scale looks just like the inverted one of the light curve, except during BJD 2455450–2455550. In particular, the spike in the amplitude variation corresponds to the luminosity dip in the light curve. This means that the *absolute* amplitude of negative superhumps would stay more or less in constant in time, independent of the

intrinsic variation of the disk luminosity. The amplitude does not change so much in the flux scale as seen in the third panels of Figures 1 and 2, although it becomes a little smaller during brightening. This supports the picture that the source of negative superhumps is the change in the luminosity of the bright spot as the gas stream sweeps on the tilted disk surface, as proposed by Wood et al. (2000) and Wood and Burke (2007). It is not known why the amplitude of negative superhumps during BJD 2455450–2455550 violently varied both in magnitude scale and in the flux scale.

We also explore the time evolution in hump profiles. The light curve profiles of negative superhumps in 28 cycles of IW And-type phenomena are exhibited in the left panels of Figures E1–E28 in the supplementary information. Here we pick up one panel among them and show it in the left panel of Figure 3 as an example of the light curve profiles. We denote the phase of negative superhumps as  $\varphi_n$  to distinguish it from the phase of orbital signal,  $\varphi_o$ , and that of super-orbital modulations,  $\varphi_s$ . As discussed above, the light source of the negative superhumps is most likely due to variable luminosity of the bright spot of the gas stream which sweeps over the face of the tilted disk as the secondary star moves around (Wood and Burke 2007). As seen in the left panel of Figure 3, the light curve of negative superhump is always single-peaked, which would mean that the bright spot formed on the back face of the disk is hidden by the optically-thick disk from observers as discussed in Wood and Burke (2007). Wood and Burke (2007) presented their simulated light curves in which the variation is approximately single sinusoidal with phase (their Fig. 3); however, they did not give any explanation for why the light curve is not flat when the stream impact point is behind the disk. Kimura et al. (2020) calculated the single-particle trajectory of the gas stream from the  $L_1$  point and determined the position of the disk surface where the gas stream hits in the tilted disk. In such a picture, the expected hump profile of negative superhump would consist of a half sinusoid in one half of the period together with the flat-bottom profile in the other half, because the bright spot on the backside is invisible to observers in the optically-thick disk. The observational light curve of negative superhumps contradicts with this simple picture as the flat-bottom profile was never observed.

The key to understanding these phenomena would be the gas-stream overflow. As the gas stream collides with the outer disk rim, some part of the stream matter overflows the disk outer edge even in the non-tilted disk (Armitage and Livio 1998; Kunze et al. 2001), and reaches the vicinity of the Lubow-Shu radius (Lubow and Shu 1975). The main part of gas stream collides with the disk outer edge, and the remnant part of the stream flows over both above and below the disk edge and reaches the inner disk. As shown in subsection 3.4.3, the tilt angle of the disk in this system is lower than 3 deg. In the

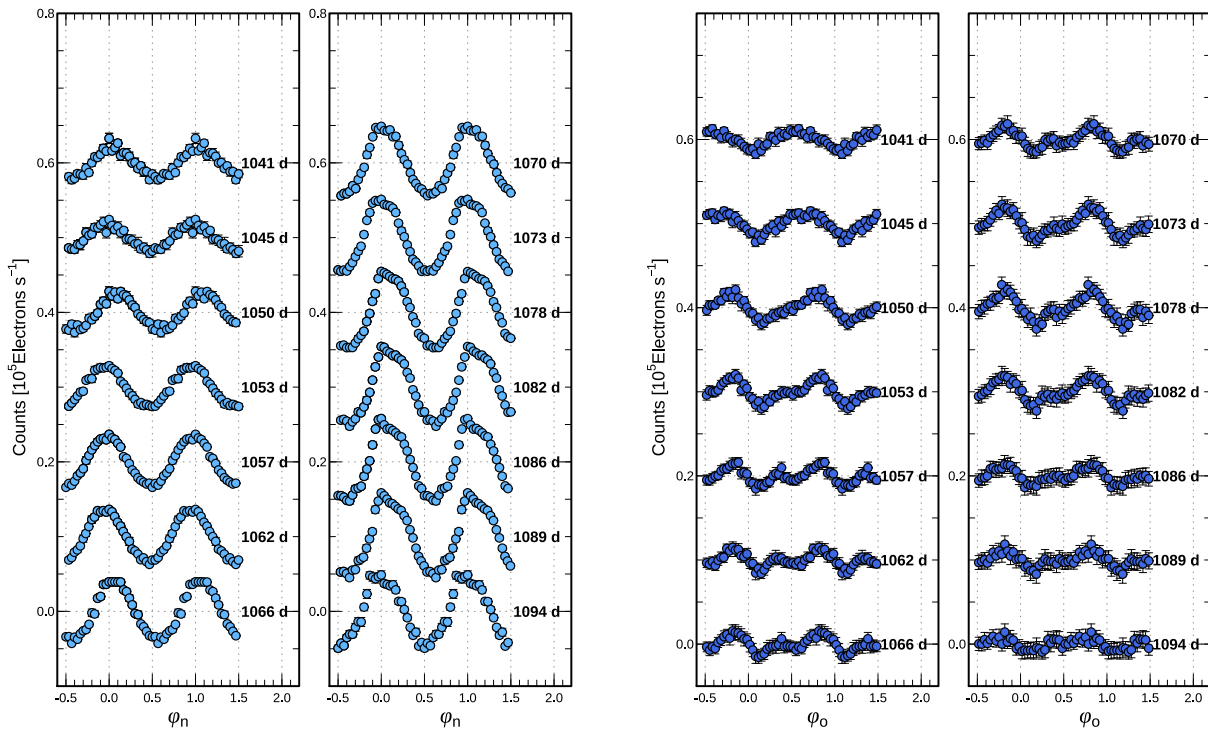


**Fig. 3.** Time evolution of phase-averaged profiles of negative superhumps and orbital signals during BJD 2456042–2456098 (cycle 24 in Figure 1). In constructing these profiles, we have folded light curves with the superhump period and the orbital period for an interval of 12.7-d (the window) and have repeated it by shifting the window by a 4-d time step. The number at the right side of each profile represents the date at the center of each window. To obtain the orbital profile, we have used the epoch of BJD 2456404.971. Some offsets are added to each profile for visibility in the vertical direction.

slightly tilted disk with such a low tilt angle, most of the gas stream may collide with the disk outer edge. However, the fraction of the overflowing matter going to the upper face of the disk will vary against that going to the lower face with the superhump period as the secondary orbits around the disk. The profile and the amplitude of negative superhumps are probably determined by how much of the gas stream overflows above the disk edge at each phase of negative superhumps, and they depend most likely on the change in the thickness of the outer disk rim and/or the tilt angle of the disk. This model of the gas-stream overflow seems to be consistent with a rich variety in the profile such as sinusoidal curves, flat-top shapes, triangular waveforms, and so on. The small decrease in the amplitude of negative superhumps in the flux scale during brightening may originate from the small increase in the thickness of the outer disk at the brightening stage, as more of the gas stream will be intercepted at the disk edge.

### 3.3 Orbital signals

In this subsection, we discuss the orbital light curve in detail. To do so, it is the most important to determine the orbital period and the binary orbital phase accurately. This system, KIC 9406652, is very advantageous in this respect because there

exists almost continuous Kepler data extending over  $\sim 1500$  d together with the spectroscopic data provided by Gies et al. (2013). The spectroscopic data were obtained within the period overlapping with the Kepler data, thanks to Gies et al. (2013). We have first estimated the orbital period to be 0.2545094(7) d from all of the Kepler data by PDM. The PDM result is displayed in the upper panel of Figure 4. We have also estimated the epoch of the inferior conjunction of the secondary star to be BJD 2456404.971 by fitting the radial velocity (RV) curve by a sinusoidal curve based on the data given in Table 2 of Gies et al. (2013). Hereafter we define the epoch of the inferior conjunction of the secondary to be the orbital phase 0.0. The lower panel of Figure 4 shows the phase-averaged profile of the light curves folded with the estimated orbital period and epoch. The accumulated error in the orbital phase over  $\sim 1500$  d is estimated to be  $\sim 0.06$ , which is less than 0.1, when considering the 95% confidence interval of the estimate of the orbital period, so that we can discuss the orbital phase with confidence for the data extending over  $\sim 1500$  d.

As demonstrated below, the light sources of the orbital signal consist of three components, that is, (1) the orbital hump due to the bright spot formed at the outer disk rim, (2) the irradiation of the secondary star by the tilted disk and/or the WD, (3) the ellipsoidal modulation of the secondary star. The orbital

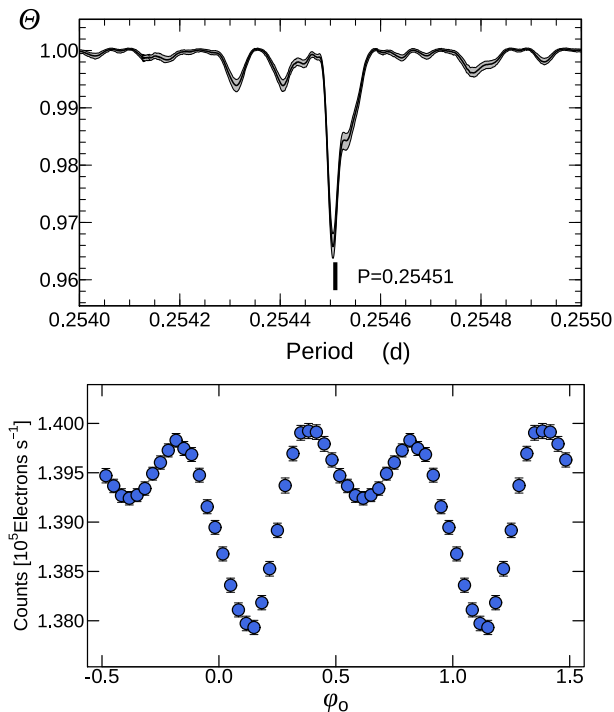


**Fig. 4.** Orbital signals in KIC 9406652. (Upper)  $\Theta$ -diagram of our PDM analysis. The area of gray-scale represents  $1\sigma$  errors. (Lower) Phase-averaged profile.

hump due to the bright spot at the disk rim is the most conspicuous feature in the optical light curve of CVs with high orbital inclination (see e.g., Krzeminski 1965). It is caused when the bright spot is on the side of the disk facing the observer, peaking at the orbital phase  $\varphi_o = 0.8\text{--}0.9$ , and it takes a half sinusoidal waveform. Hereafter  $\varphi_o$  signifies the orbital phase. If the disk is tilted, the surface of the secondary will be more irradiated by the accretion disk than the otherwise case, because the inner hot part of the disk would be easily exposed to the surface of the secondary. The flux variation by the source (2) is predicted to peak around  $\varphi_o = 0.5$  since the irradiated hemisphere of the secondary is directly facing the observer at the superior conjunction of the secondary. The flux variation by the source (3) peaks at 0.25 and 0.75 in the orbital phase. We give a schematic picture of the orbital motion of the secondary star and the tilted disk in Figure 5 for the binary parameters corresponding to KIC 9406652, i.e., a Roche-lobe filling semi-detached binary with the mass ratio  $q = M_2/M_1 = 0.83$  and the orbital inclination,  $i = 50$  deg.

We first consider the effect of ellipsoidal modulations. We can approximately estimate this effect as follows. The ellipsoidal variation of a Roche-lobe filling secondary star is calculated by using the numerical code described in detail by Hachisu and Kato (2001). As for the input parameters in this code, we adopt that the temperature of the secondary, the inclination of the binary system, the WD mass, and the binary mass ratio are

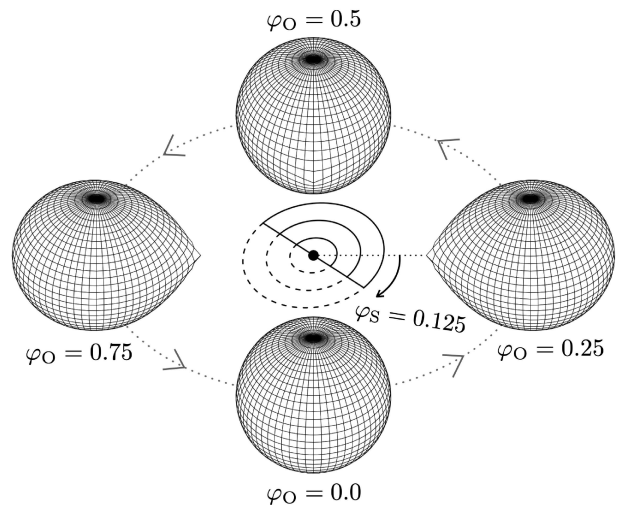


**Fig. 5.** Schematic figure of the orbital motion of the secondary star and the retrogradely precessing tilted disk in KIC 9406652. The inclination angle is assumed to be 50 deg. The central black point represents a WD and we put a tilted disk at the center with the tilt angle of 10 deg for visibility. The nodal line is indicated by a diametric line passing the central WD. The secondary orbits counterclockwise around the central WD and the tilted disk precesses clockwise. The solid and dashed lines represent the concentric rings of the tilted disk above and below the orbital plane, respectively. The phases,  $\varphi_s$  and  $\varphi_o$ , stand for that of the precession of the tilted disk (or that of the super-orbital modulation) and the orbital phase, respectively. The phase zero for  $\varphi_s$  is defined when the nodal line of the tilted disk is perpendicular to the line of sight and the front face of the tilted disk turns towards the observers. The phase of the tilted disk shown in this figure is 0.125. The orbital phase zero is defined when the secondary star is at the inferior conjunction.

4500 K, 50 deg,  $0.9 M_\odot$ , and 0.83, respectively, according to Gies et al. (2013). The resultant ellipsoidal modulation is displayed in the upper panel of Figure 6. We use the following equation to estimate the flux variation by the ellipsoidal effect.

$$F_{\text{ellip}} = F_{\text{mean}} \frac{F_2}{F_{\text{disk}} + F_2} \left( 10^{\frac{\Delta m}{-2.5}} - 1 \right). \quad (3)$$

Here  $F_{\text{mean}}$ ,  $F_2$ ,  $F_{\text{disk}}$ , and  $\Delta m$  are the mean observational flux, the flux of the secondary, the flux of the disk, and the variation of the model light curve for the ellipsoidal effect in the magnitude scale, respectively. To evaluate  $F_2/(F_{\text{disk}} + F_2)$ , we use the spectral energy distribution given in Figure 10 of Gies et al. (2013). These authors reported that  $F_2/F_{\text{disk}}$  is 0.04(1) at  $5400\text{\AA}$ . The value of  $F_2/F_{\text{disk}}$  through the *Kepler* response function is then calculated to be 0.06(2). We adopt the average value, 0.06, as  $F_2/F_{\text{disk}}$ .<sup>2</sup>

We can now subtract the ellipsoidal effect from the orbital profile by using equation (3). After subtracting the estimated ellipsoidal effect, the orbital light curve given in the lower panel of Figure 4 is then modified to that shown in the lower panel of Figure 6. The ellipsoidal effect is only a few percent of the entire orbital variation and the major part of the orbital signal comes from the orbital hump and the irradiation effect.

<sup>2</sup> Actually,  $F_2/F_{\text{disk}}$  changes with time, but we neglect its time variation.

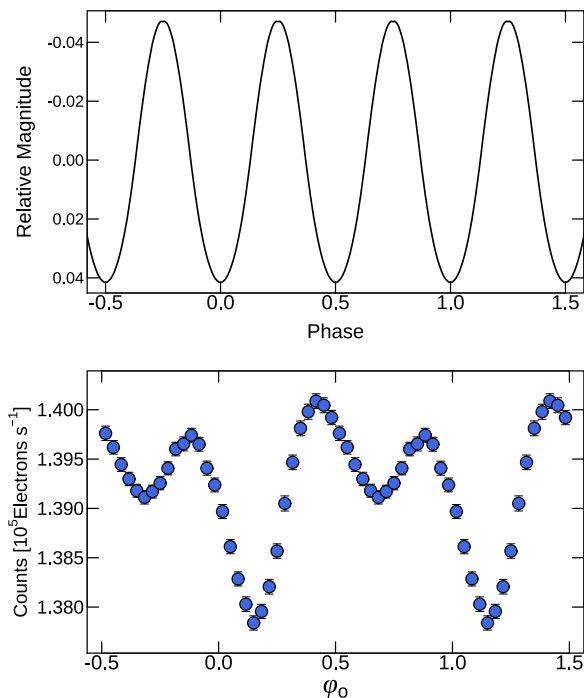


**Fig. 6.** (Upper) Model light curve of ellipsoidal modulations of the secondary having 4500 K in the system with the inclination of 50 deg. (Lower) Phase-averaged profile of overall orbital signals after the subtraction of the ellipsoidal effect.

Nevertheless, we can confirm that the two peaks around 0.4–0.5 and 0.8–0.9 become clearer after the subtraction. In particular, the peak around 0.4–0.5 becomes higher, and the peak around 0.8–0.9 slightly shifts towards the orbital phase 1.0. As expected, the former is due to the irradiation of the secondary star and the latter is due to the bright spot at the disk rim.

Since no light variation of the secondary star itself is expected to occur, it is thought that the light variation due to the ellipsoidal effect is not variable in time. On the other hand, the light variations due to the other two sources, (1) the orbital hump by the bright spot and (2) the irradiation of the secondary, vary with time because they depend on the disk geometry and the disk luminosity. By utilizing their time variations, we can isolate one component from the other. We have investigated the time evolution of the orbital light profiles in almost the same way as we have done for negative superhumps and display them in the right-hand panels of Fig. E1–E28 in the supplementary information for 28 cycles of the IW And-type phenomenon. The width of the window used is  $50 \times P_{\text{orb}} \simeq 12.7$  d, which is the same as that in the case of negative superhumps.

It is expected that the orbital hump by the bright spot will dominate when the disk is not tilted. We have confirmed this as light curves were those with a single peak at  $\varphi_0 = 0.8 - 0.9$  when negative superhumps were almost invisible or very weak in the earliest phase of the light curve in the top panel of Figure

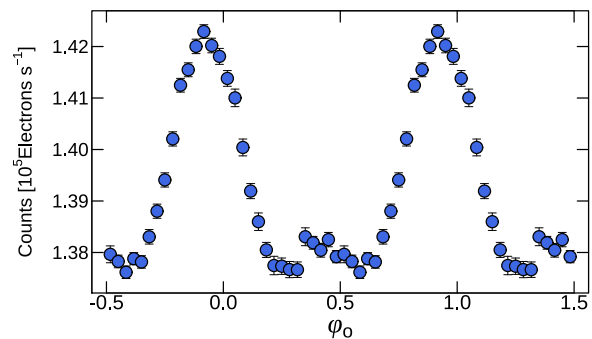


**Fig. 7.** Phase-averaged profile of orbital signals during BJD 2454964–2455020.

1 (see also Fig. E1 and E5). Figure 7 shows the orbital profile derived from the data during BJD 2454964–2455020, which is the earliest part of the observational data. This light curve profile is close to the half sinusoidal wave, a typical orbital hump light curve due to the bright spot.

On the other hand, when negative superhumps are clearly visible and so the disk is thought to be tilted, the orbital light curve becomes very complex as both the bright spot and the irradiation of the secondary contribute to them (see Fig. E2–E4, E7–E9, and E12–E27). We give an example of the profile variation during one cycle (cycle 24) of the IW And-type phenomenon in the right panel of Figure 3. We find that the peak around the orbital phase 0.4–0.5, which is thought to originate from the irradiation, becomes dominant when the system brightens (at the brightening phase of the IW And-type light variation). Figure 8 exhibits the phase-averaged profiles at brightening, quasi-standstills, and dips for about 1000 d (BJD 2455296–2456312), over which sustained negative superhumps were confirmed. The data of brightening, quasi-standstills, and dips have count rates more than  $1.8 \times 10^5$ , between  $0.9 \times 10^5$  and  $1.8 \times 10^5$ , less than  $0.9 \times 10^5$ , respectively. We see that the irradiation effect appearing at  $\varphi_0 = 0.5$  becomes more dominant when the system becomes brighter, while the peak around phase 0.8–0.9 becomes remarkable when the system becomes fainter. The major part of the profile at the brightening stage would originate from the irradiation effect, and the orbital hump is the strongest at dips. The profile at quasi-standstills is the intermediate one between the other two. These observations are consistent with our expectation that the secondary star will more easily be irradiated by the WD and the disk when the disk is tilted, and that more flux will illuminate the secondary when the disk becomes brighter. The light maximum seems to be shifted slightly from phase 0.5 to the early phase especially during quasi-standstills (see the lower panel of Figure 8). This could be because the irradiated region on the surface of the secondary may be asymmetric to the line connecting the WD and the secondary as a part of irradiating radiation from the disk and



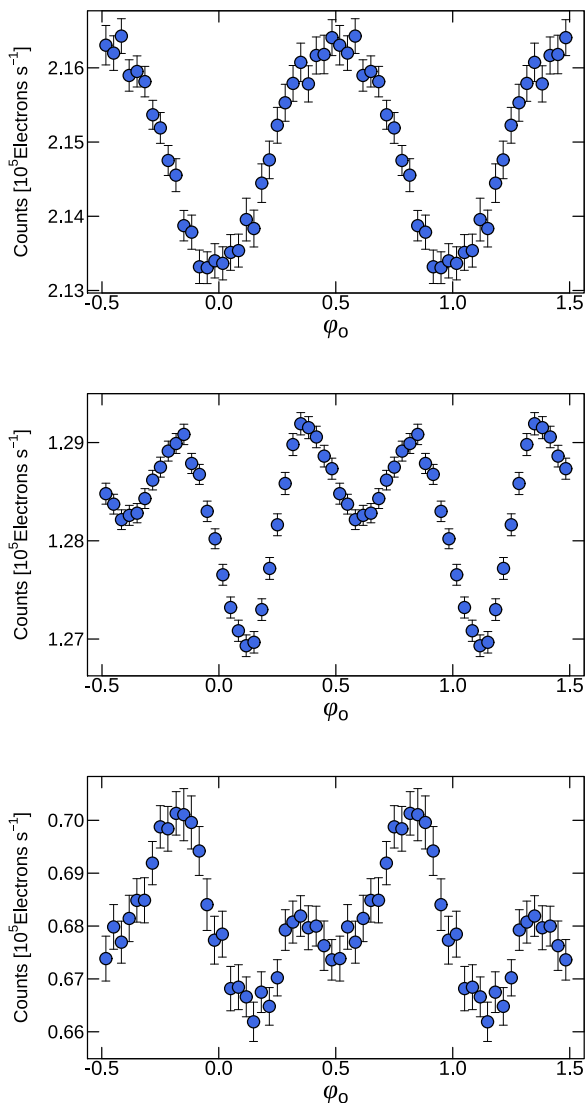


**Fig. 8.** Phase-averaged profiles of orbital signals during BJD 2455296–2456312. (Upper) Profile during brightening. (Middle) Profile during quasi-standstills. (Lower) Profile during dips.

the WD may be intercepted by the gas stream itself or a flared disk rim where the gas stream first collides.

Gies et al. (2013) have constructed orbital light curve from *Kepler* observation quarters 1 to 4 and they have noticed that it resembles that of a low-amplitude ellipsoidal binary light curve with two unequal minima. However, they have chosen the epoch phase arbitrarily. Since we have determined the orbital period and the epoch of this system quite accurately, we can study the orbital light curve for the same interval as that of Gies et al. (2013). Figure 9 illustrates the orbital light curve for the same interval constructed based on the period, 0.2545094 d, and the epoch, BJD 2456404.941, as the phase zero for the inferior conjunction of the secondary star in our analysis, together with that based on the orbital period and the epoch reported by

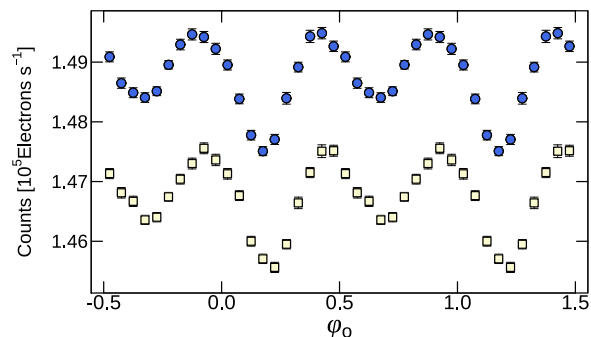


**Fig. 9.** Phase-averaged profile during the *Kepler* quarters 1–4. The upper light curve profile (shown in dots) is that constructed based on the period and the epoch estimated in this paper and the lower one (shown in squares) is that based on the period and the epoch estimated in Gies et al. (2013), where the latter is shifted by  $-0.02 \times 10^5 \text{ e}^- \text{ s}^{-1}$  from the former.

Gies et al. (2013)<sup>3</sup>. We see that the difference in the phase of the two light curves is less than 0.05, which is reasonable as the orbital period reported by Gies et al. (2013) is consistent with that of our estimate within the 95% confidence level. This indicates that the orbital phase determined in our analysis may be reliable over  $\sim 1500$  d. Although they have stated that it resembles that of an ellipsoidal binary light curve, we see from Figure 9 that the phases of the double peaks do not match those of the ellipsoidal modulation. In addition, the two peaks did not necessarily appear simultaneously. One peak appeared sometime in one orbital cycle and the other peak appeared in other time (see Fig. E1–E5), and we find clear double peaks only after folding light curves for all cycles. We thus conclude that the apparent double peaks are very unlikely to be due to the ellipsoidal modulation of the secondary but rather due to the superposition of the irradiation of the secondary and the orbital hump.

One might ask why the bright spot was still visible in the orbital light curve when the disk was apparently tilted, as negative superhumps and orbital signals are more or less mutually exclusive to each other in other stars (see, e.g., Osaki and Kato 2013). This is probably because the tilt angle was rather low as shown in subsection 3.4.3 and the orbital inclination was relatively high in KIC 9406652. When the disk is slightly tilted, some part of the gas stream would overflow the outer disk edge, while some other part of the gas stream would collide with the disk rim as discussed in the previous subsection. The bright spot is thus formed at the disk rim in this case even if the disk is tilted and it is observable as the orbital hump if the inclination is sufficiently high. The objects reported by Osaki and Kato (2013) would have small inclination angles and/or highly tilted disks.

<sup>3</sup> As for the epoch, we averaged the 4 values of  $T$  in Table 3 in Gies et al. (2013)

### 3.4 Super-orbital modulations

#### 3.4.1 Frequency variations

This object exhibited super-orbital light modulations with a  $\sim 4$ -d period besides negative superhumps when negative superhumps appeared (Gies et al. 2013). We first discuss frequency variations of super-orbital modulations. The super-orbital light modulation is thought to be produced by variations in the projected area of the disk to the line of sight as the nodal line of the tilted disk precesses retrogradely. On the other hand, negative superhumps are produced by variations in the luminosity of the bright spot, which is in turn produced by the gas stream sweeping on the tilted disk surface as described in subsection 3.2.3. The period of negative superhumps is given by the synodic period between the retrogradely precessing tilted disk and the orbiting secondary star. Although these two phenomena are observationally completely independent, their frequencies are related to each other, i.e., by the relation  $f_{\text{sup}} = f_{\text{NSH}} - f_{\text{orb}}$ , where  $f_{\text{sup}}$ ,  $f_{\text{NSH}}$ , and  $f_{\text{orb}}$  denote the frequencies of super-orbital modulations, negative superhumps, and orbital signals, respectively, and correspond to  $f_1$ ,  $f_3$ , and  $f_2$  in Gies et al. (2013). In addition,  $f_{\text{sup}}$  stands for  $|\nu_{\text{hPR}}|$  as defined in subsection 3.2.2 (see also equation (1)). This means that we can examine the variation of nodal precession rates by two different methods, i.e., the direct observation of the period of super-orbital modulations and the indirect way from the frequency of negative superhumps.

We here derive the frequency variation of super-orbital modulations during BJD 2455296–2456312 by PDM. The effects of negative superhumps and orbital signals are removed in advance from the original light curves by using the results obtained before and the long-term overall trend of the processed light curves is subtracted by LOWESS (see subsection 2.2). We display an example of this process in Figure 10 for cycle 24 of the IW And-type phenomenon, which is defined in Figure 1. The top light curve (shown by black dots) in Figure 10 is the original light curve, and the second one (gray dots) is the light curve where the effects of negative superhumps and orbital signals are removed. The third one (orange dots) is the normalized light curve in which the long-term overall trend is subtracted. The bottom one is the resultant one where all three effects: negative superhumps, orbital signals, and super-orbital modulations are subtracted and we will explain it later. We have applied PDM to the normalized light curve with a 120-d window and repeated it by shifting it by 20 d, as we did in subsection 3.2.2, and have derived the frequency of super-orbital modulations. We also have derived the frequency variation of negative superhumps by PDM with the same window size of 120-d and the same time step of 20-d. Results for  $f_{\text{sup}}$  and  $f_{\text{NSH}} - f_{\text{orb}}$  are exhibited as the triangles and circles in the third panel of Figure 11, respectively. Here we use the orbital frequency,  $f_{\text{orb}} = 3.929128 \text{ d}^{-1}$ , estimated in subsection 3.3. We see that these

two frequencies vary in unison, thus confirming their common origin.

To put it in another way, we can determine the orbital frequency from these two observed frequencies ( $f_{\text{sup}}$  and  $f_{\text{NSH}}$ ) by assuming it as an unknown with the least-squares method. The result is displayed in Figure 12 where the best-fit orbital period is determined to be 0.254514(7) d. This value is consistent within its  $1\sigma$  error with the orbital period estimated in subsection 3.3.

The period of the super-orbital modulations increases or decreases by  $\sim 0.1$  d on timescales of a few hundred days, which means that the radial mass distribution and/or the disk radius varies on long timescales according to equation (1). The  $O - C$  curve of super-orbital modulations is displayed in the top panel of Figure 11 and the  $O - C$  values are summarized in Table E7. The moderate variation in the  $O - C$  curve reflects the variation of  $f_{\text{sup}}$ .

#### 3.4.2 Amplitude and profile variations

We here discuss the amplitude variation of super-orbital modulations. As shown in Figure 10, we have subtracted the long-term overall trend of the light curves for data analyses; however, it is thus not easy to discern an individual cycle of the super-orbital modulation from the intrinsic variation of the disk, because the time scales of these two phenomena are sometimes very similar, particularly during quasi-standstills. The intrinsic variation could amplify and/or weaken super-orbital modulations. In estimating the amplitude of super-orbital modulations, we remove a part of data in which the intrinsic variation is violent (mainly around brightening) like the data around 1040–1060 d in Figure 10 since we could not subtract it well.

When deriving the time variation of the semi-amplitude of super-orbital modulations, we first divide the data during BJD 2455296–2456312 into 21 intervals having  $\sim 30$ –60-d lengths to lower the error. We then determine the period of super-orbital modulations,  $P_{\text{sup}} = 1/f_{\text{sup}}$ , for each interval from the frequency of negative superhumps,  $f_{\text{NSH}}$ , by using the relation  $f_{\text{sup}} = f_{\text{NSH}} - f_{\text{orb}}$ . This is because the direct determination of  $P_{\text{sup}}$  around 4 days is difficult for such a short interval. We next create a phase-averaged profile in each time interval by folding the normalized light curve with the period that we have derived. Finally, we fit each profile with the equation  $a \cos(2\pi(\varphi - b)) + 1$ , where  $\varphi$  is the phase of super-orbital modulations, since super-orbital light modulations resulting from the variation in the projected area of the tilted disk are supposed to have the sinusoidal waveform (see, equation (5) in the next subsection). Here  $a$  and  $b$  are unknown constants to be fitted to the light curve, and  $a$  stands for the semi-amplitude of super-orbital modulations and  $b$  represents the epoch of its light maximum, respectively. The results of the regressions are summarized in Table E8. The phase-averaged profile of super-

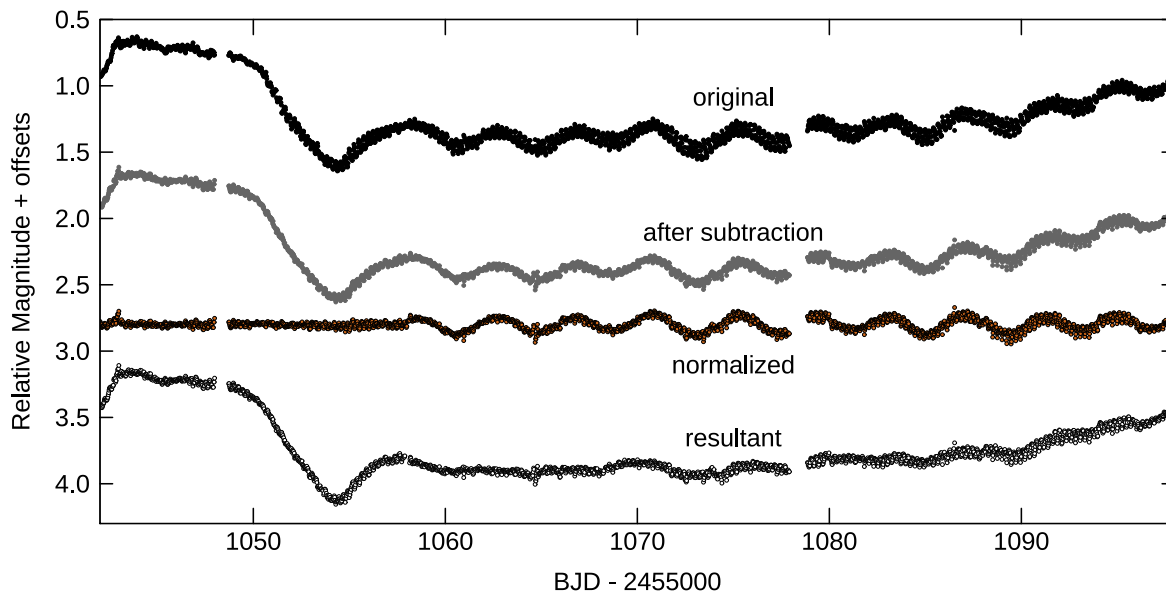


**Fig. 10.** Example of the process of the subtraction of the effects of negative superhumps, orbital signals, and super-orbital modulations from the original light curve in the case of cycle 24. The top light curve (shown by the black dots) is the original light curve and the second one (the gray dots) is that where the effects of negative superhumps and orbital signals are subtracted (shifted by 1 mag for visibility). The third one (the orange dots) is the normalized light curve where the long-term trend is subtracted from the second one (shifted by 2.8 mag). The bottom one (the open dots) is the resultant light curve where the all effects (superhumps, orbital signals, and super-orbital modulations) are subtracted from the original light curve (shifted by 2.5 mag).

orbital modulations and their semi-amplitude in each interval are exhibited in Figure 13 and the fourth panel of Figure 11, respectively. We now introduce the phase of the nodal precession,  $\varphi_s$ , in such a way that the phase zero corresponds to the light maximum of super-orbital modulations, i.e.,  $\varphi_s = \varphi - b$ , which is counted clockwise in Figure 5 because the disk precesses retrogradely, i.e.,  $\nu_{\text{nPR}}(t) = -f_{\text{sup}}$ . We have confirmed just in case that the semi-amplitude of periodic light variations having the super-orbital period in the time intervals during which negative superhumps were not clearly observed was less than the smallest one during the interval when negative superhumps were clearly detected.

We see from the fourth panel of Figure 11 and Figure 13 that the semi-amplitude varies quite rapidly. As expected, some of the profiles tend to have sinusoidal shapes when their amplitudes are large (i.e., at 799 d, 1078 d, and 1138 d in Figure 13 where the dates are counted from BJD 2455000). On the other hand, some of them greatly deviate from the sinusoidal curve when their amplitudes are small (i.e., at 665 d, 710 d, 895 d, 938 d, 981 d, and 1289 d in the same figure). It would be difficult to completely remove the intrinsic variation of the accretion disk from super-orbital light variations, as expected. Although the estimate of the parameter  $b$  differs among 21 intervals (see Table E8), this difference does not necessarily indicate that the orientation of the disk tilt is reset to new values with each cycle of the IW And-type phenomenon. This is because many factors such as the data gap, the remnant of the intrinsic variation of the

accretion disk, and the difference in the period with which each set of light curves is folded could affect the results.

Now we can approximately recover the light curve purely originating from the accretion events by subtracting the three effects: negative superhumps, orbital signals, and super-orbital modulations, from the original light curves. We show the corrected light curve, in which all those three effects, are removed in the second panel of Figure 11 and also in the bottom light curve of Figure 10. We see that the oscillatory variations still remain in quasi-standstills after the subtraction of super-orbital modulations: a common feature of IW And-type DNe (e.g. Szkody et al. 2013; Kato et al. 2020).

### 3.4.3 Estimation of the tilt angle of the disk

Finally, we estimate the tilt angle of the disk by using the semi-amplitude variation. If we write the angle, which the line of sight and the normal vector of the flat disk make, as  $\alpha$ , the disk flux from the observer is then written by  $F_{\text{disk}} \cos \alpha$ , where  $F_{\text{disk}}$  is the disk flux seen from pole-on. Let us consider that the disk is tilted out of the orbital plane and its normal line rotates around the normal of the binary orbital plane retrogradely, i.e., retrograde precession of the tilted disk. The tilt angle,  $\theta$ , is defined by an angle between the normal of the orbital plane and the normal of the tilted disk. We further write the azimuthal angle of the tilted disk at a certain instance by  $\phi$ , where  $\phi$  is measured from the direction of the line of sight. We note here that the azimuthal angle of the tilted disk,  $\phi$ , and the phase of super-orbital

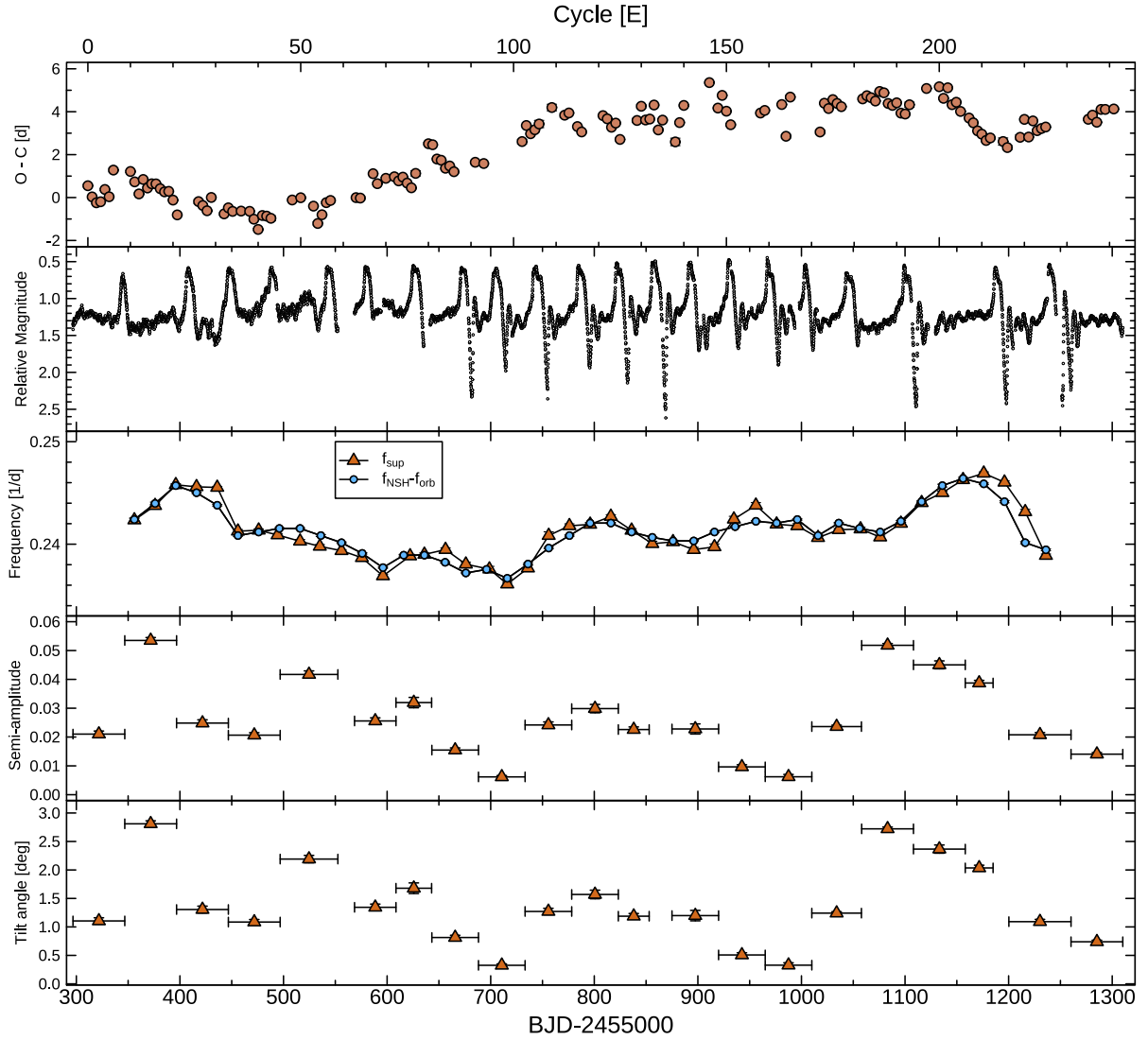


**Fig. 11.** Results of analyses of super-orbital modulations in KIC 9406652. The top panel is plotted against the cycle number  $E$  and the other panels are plotted against BJD, respectively. (Top)  $O - C$  curve of the light maxima. The assumed period is 4.128 d, and the epoch is BJD 2455298.275, respectively. (Second) Predicted light variations originating from the accretion process. We derived them by subtracting super-orbital modulations, negative superhumps, and orbital signals and binning them per 0.1 d. (Third) Frequency variations. The triangles and circles stand for the frequency of super-orbital modulations ( $f_{\text{sup}}$ ) and the frequency of negative superhumps minus the orbital frequency ( $f_{\text{NSH}} - f_{\text{orb}}$ ), respectively. (Fourth) Semi-amplitude variations in units of relative flux. (Bottom) Time evolution of tilt angles of the disk estimated from the semi-amplitude variation.

modulations,  $\varphi_s$ , are related to each other by  $\phi = 2\pi\varphi_s$ .

We consider a spherical triangle made by the three directions, the normal of the orbital plane, the line of sight, and the normal of the tilted disk. By applying the cosine law of the spherical trigonometry to this, we obtain

$$\begin{aligned} \cos \alpha &= \cos i \cos \theta + \sin i \sin \theta \cos \phi, \\ &= \cos i \cos \theta (1 + \tan i \tan \theta \cos \phi), \end{aligned} \quad (4)$$

where  $i$  is the inclination angle of the binary system. If the intrinsic flux of the disk and the flux of the secondary star are denoted as  $F_{\text{disk}}(t)$  and  $F_2$ , respectively, the observed flux is written as

$$\begin{aligned} F_{\text{disk}}(t) \cos \alpha + F_2 = & \\ (F_{\text{disk}}(t) \cos i \cos \theta + F_2) \left( 1 + \frac{\tan i \tan \theta}{1 + \frac{F_2}{F_{\text{disk}}(t) \cos i \cos \theta}} \right) \cos(2\pi\varphi_s), & \end{aligned} \quad (5)$$

where the time dependence of the intrinsic disk flux is taken into account by  $F_{\text{disk}}(t)$ . We have normalized the light curves by  $F_{\text{disk}}(t) \cos i \cos \theta + F_2$  and the semi-amplitude  $a$  introduced in the previous subsection corresponds to  $\tan i \tan \theta / (1 + \frac{F_2}{F_{\text{disk}}(t) \cos i \cos \theta})$ . According to Gies et al. (2013), we set  $i = 50$  deg and used 0.06 for  $F_2/F_{\text{disk}}(t)$  as in subsection 3.3.<sup>4</sup> We

<sup>4</sup> Actually,  $F_2/F_{\text{disk}}(t)$  depends on the time variation of the disk luminosity, but we here neglect that variation as did in Sec. 3.3.

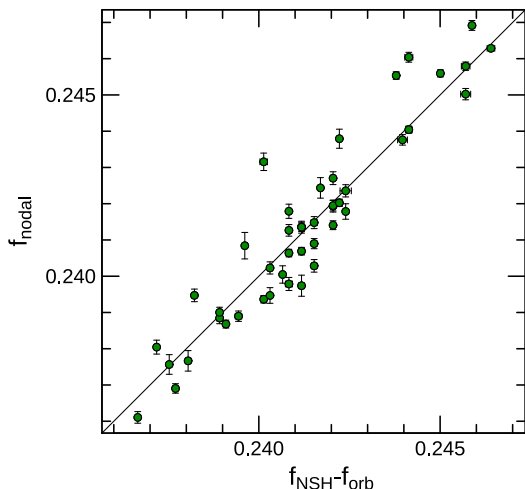


**Fig. 12.**  $f_{\text{nodal}}$  vs.  $f_{\text{NSH}} - f_{\text{orb}}$  displayed in the third panel of Fig. 11. Ideally the points are on the solid line.

can now calculate the tilt angle.

The estimated tilt angle is given in the bottom panel of Figure 11. It is less than 3 deg in KIC 9406652 in the case of a 50-deg inclination. Smak (2009) estimated the tilt angles of several CVs showing super-orbital modulations by using basically the same method and obtained the tilt angles around 3–4 deg on average. Our results seem to be consistent with his results. Besides, we have already used the evidence of a relatively low tilt angle to interpret the light curve profile of negative superhumps in subsection 3.2.3 (see also the left panel of Figure 3). Although there is a possibility that the tilt angle in KIC 9406652 is underestimated because of the intrinsic variation of the disk as mentioned in subsection 3.4.2, the tilt angle unlikely exceeds 6 deg when considering the typical thickness of the disk outer edge ( $h/r \sim 0.1$  at the outer disk edge, where  $h$  stands for the scale height; Smak 1992).

From Figure 11, we find three peaks in the tilt angle around 370 d, 520 d, and 1100 d together with a local maximum around 800 d where dates are counted from BJD 2455000. When comparing this with the third panel of Figure 1, we see a weak correlation between the tilt angle and the amplitude of negative superhumps in the sense that the amplitude of negative superhumps is larger when the tilt angle is higher. We also find a weak correlation between the tilt angle and the cycle length of the IW And-type phenomenon when both negative superhumps and super-orbital modulations were clearly detected, in the sense that the duration of quasi-standstills tends to become longer as the tilt angle becomes higher, by comparing the second and bottom panels of Figure 11.

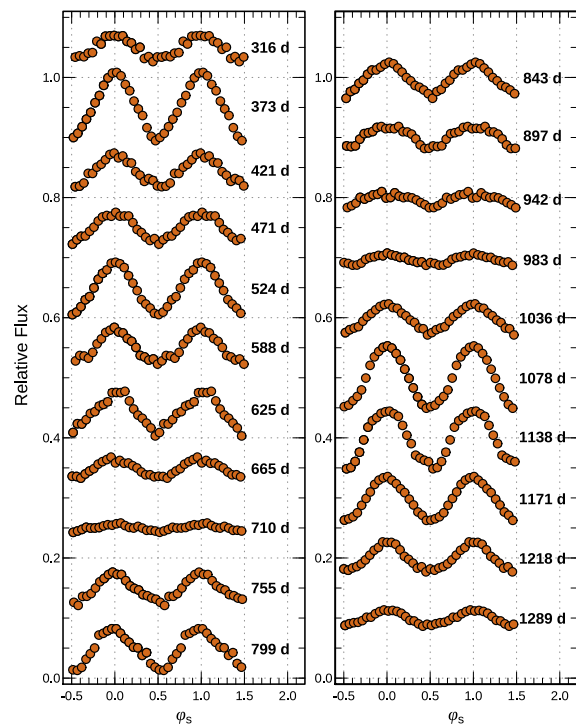


**Fig. 13.** Time evolution of profiles of super-orbital modulations in KIC 9406652. We here fold the light curves normalized by the averaged flux. The window size is  $\sim 30$ –60 d. The number at the right side of each profile is the date at the center of each window. Some offsets are added to each profile for visibility in the vertical direction.

### 3.5 Irradiation of the secondary star and the orientation of the tilted disk

We have shown in subsection 3.3 that the irradiation of the secondary plays a major role in the orbital light curve when the disk is tilted, in particular when the system is in the brightening stage (see Figure 8). In this subsection, we examine how the orbital light curve looks if we divide the observational data with respect to the phase of the super-orbital modulation  $\varphi_s$ , i.e., with the orientation of the tilted disk to the line of sight. The data used here are restricted to those in the brightening stage during BJD 2455296–2456312 to focus on the irradiation effect. We have already determined the phase of the super-orbital modulation in subsection 3.4.2 and here divide the data into 8 short intervals with respect to  $\varphi_s$ :  $\varphi_s \sim 0.0$  (with  $-0.0625$ – $0.0625$ ),  $0.125$  (with  $0.0625$ – $0.1875$ ),  $0.25$  (with  $0.1875$ – $0.3125$ ),  $0.375$  (with  $0.3125$ – $0.4375$ ),  $0.5$  (with  $0.4375$ – $0.5625$ ),  $0.625$  (with  $0.5625$ – $0.6875$ ),  $0.75$  (with  $0.6875$ – $0.8125$ ), and  $0.875$  (with  $0.8125$ – $0.9375$ ), respectively. We then construct 8 orbital light curves by collecting the data corresponding to each phase interval.

Figure 14 exhibits the results, and we show the orientation of the tilted disk in each figure. The amplitude of the orbital light curve is the largest around  $\varphi_s = 0.5$  while it is the small-

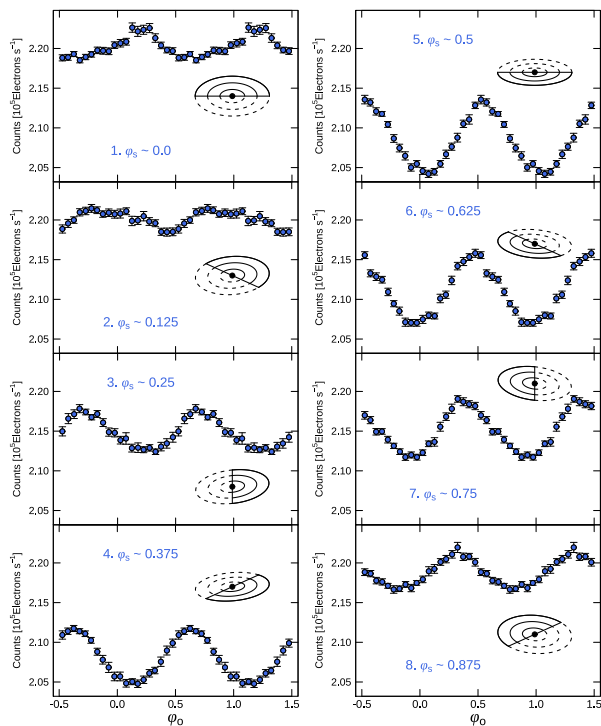


**Fig. 14.** Eight types of orbital profiles from the data limited for brightening during BJD 2455296–2456312. The inset of each figure shows the orientation of the tilted disk where the central WD is marked by the black dot and the diametric line passing the WD is the nodal line of the tilted disk. The solid and dashed lines represent the equatorial plane of the tilted disk above and below the orbital plane of the binary system, respectively. Here,  $\varphi_s$  and  $\varphi_o$  stand for the super-orbital phase and the orbital phase, respectively, as in Figure 5.

est around  $\varphi_s = 0.0$ . This is easily understood: at  $\varphi_s \sim 0.5$ , which corresponds to the right top panel of Figure 14, the near side of the tilted disk is above the orbital plane while the far side is below the orbital plane, and hence, the tilted disk and the central WD then irradiate the upper face of the secondary most strongly at the orbital phase  $\varphi_o = 0.5$  and they irradiate its lower face most strongly at  $\varphi_o = 0.0$ , as the secondary star goes around the tilted disk. Here the upper/lower face of the secondary star means the surface of the secondary above/below the orbital plane, respectively. If the orbital inclination is smaller than 50 deg, the observer sees mostly the irradiated upper face of the secondary around  $\varphi_o = 0.5$  (see also Figure 5) and thus the effect of irradiation of the secondary is maximal. The orbital profile at  $\varphi_s \sim 0.5$  shows maximum light at  $\varphi_o = 0.5$  and takes the largest amplitude. On the other hand, in the opposite case at  $\varphi_s \sim 0.0$  corresponding to the left top panel, the situation is just opposite to the case mentioned above, the upper face of the secondary is not irradiated well by the tilted disk around  $\varphi_o = 0.5$  and the irradiated upper face of the secondary is hidden around  $\varphi_o = 0.0$  from the observer. The effect of irradiation of the secondary is thus minimal at  $\varphi_s = 0.0$ .

We see furthermore from Figure 14 that the orbital phase of the light maximum moves to earlier phases as the phase of the super-orbital period,  $\varphi_s$ , advances. This means that the direction of the nodal precession of the tilted disk is retrograde as expected from the “negative” nature of negative superhumps. The variation in amplitudes and the shift of peak phases thus give us direct evidence that the disk is actually tilted out of the orbital plane and precesses retrogradely as the secondary star acts as a reflecting mirror for the irradiation by the tilted disk and the WD. Also, the irradiation on the surface of the secondary star could affect its spectrum. The spectrum of the secondary star may show a higher-temperature component during the brightening stage, which could change with orbital and super-orbital phases.

## 4 Discussion

### 4.1 Time evolution of the radius and the radial mass distribution of the tilted disk

As shown in subsection 3.2.2, the frequency of negative superhumps exhibited a characteristic variation in one cycle of the IW And-type phenomenon of KIC 9406652: a rapid decrease at the beginning of brightening followed by a small increase and a gradual increase during quasi-standstills (see the bottom panels of Figures 1 and 2). We interpret this frequency variation, introducing some results in Kimura et al. (2020). They predicted the variation in the nodal precession rate,  $\nu_{\text{NPR}}$ , given in equation (1), which is directly related to the frequency of negative superhumps by equation (2), via their numerical simulations of the thermal-viscous instability in the non-tilted and tilted disks.<sup>5</sup>

We first discuss the frequency variation at the beginning of the brightening. Generally, the disk expands at the beginning of a (small) outburst (Ichikawa and Osaki 1992) and then the frequency of negative superhump rapidly tries to increase. We see from the bottom panels of Fig. 10 and Fig. 12 in Kimura et al. (2020) that there are two patterns in its time evolution after the initial variation: a continuous increase and a rapid decrease. The latter occurs if a huge amount of mass accumulates at the outer disk and the disk reaches the tidal truncation radius. In this case, the angular-momentum loss by the tidal torque exerted by the secondary star is considered to keep being efficient for a while and a huge amount of mass accumulated in the outer disk accretes on the WD. In other words, the disk becomes more or less near the standard disk with  $\Sigma \propto r^{-3/4}$  during outburst from the quiescent disk with  $\Sigma$  having a positive slope with  $r$ . According to the second row of equation (2), the frequency of negative superhumps depends only on the weight of the disk mass in the radial direction, i.e.,  $\Sigma(r)$ , if the disk radius is fixed to the tidal truncation radius. If the weight of the mass in the

<sup>5</sup> Here the non-tilted disk model means the model in the limiting case of the lowest tilt angle.

inner disk increases, the frequency decreases. The observed rapid drop, therefore, seems to represent the rapid change of the surface-density distribution, as actually predicted in the tilted-disk model in Kimura et al. (2020). This interpretation would be consistent with the spectral energy distribution observed at the brightening stage in IW And stars, which was close to that of the standard disk (Szkody et al. 2013).

On the other hand, the observed gradual increase in the frequency during the quasi-standstill is against the prediction by Kimura et al. (2020). In their tilted disk models, the outer part of the disk is supposed to be in the cool state during the quasi-standstill. The addition of matter at the disk edge by the gas stream (having less specific angular momentum than that of the disk edge) causes contraction of the disk radius, which leads to a gradual decrease in the nodal precession rate, i.e., the frequency of negative superhumps. The gradual increase in the negative-superhump frequency in the observations thus suggests the gradual increase in the disk radius. The disk expansion during standstills was already suggested in NY Ser, an SU UMa-type star by Kato et al. (2019). This object entered a standstill in 2018 after frequent normal outbursts, which were terminated by a superoutburst. In order for a superoutburst to start, the disk radius must reach the 3:1 resonance radius at the beginning of the superoutburst (Osaki 1989), and thus the disk radius should have gradually increased during standstills. Kato (2019) suggested that the same situation could occur in the case of IW And-type stars as well.

It seems difficult to realize a gradual increase in the disk radius during the quasi-standstill. The outer part of the disk must be in the hot state in order for the disk radius to expand. However, if the disk is in the hot state under a condition of weak tidal torques (i.e., its radius is below the tidal truncation radius), the disk would then expand rapidly and it could not stay in the quasi-steady state for a long while. The gradual increase in the negative-superhump frequency, which is suggested by observations during the quasi-standstill, poses a new question about the nature of the quasi-standstill in IW And-type stars, to which we do not have any immediate answers.

## 4.2 Examination of the models for the IW And-type stars

As mentioned in the introduction, two models have been proposed so far to explain the characteristic light variation in IW And stars. We first examine the mass-transfer-burst model proposed by Hameury and Lasota (2014) by using our results. Although they did not discuss the disk radius variation in their paper, the mass transfer burst from the secondary would lead to a sudden contraction of the disk radius (see Ichikawa and Osaki 1992). This phenomenon may seem to be consistent with the observed sudden drop in the frequency of negative superhumps,

which occurred at the beginning of brightening. However, their model is inconsistent with our present results in other aspects. As demonstrated in subsection 3.2.3, the light source of negative superhumps is the bright spot of the gas stream sweeping on the surface of the tilted disk. If 10-times increases in mass transfer rate are needed to reproduce the brightening as predicted by Hameury and Lasota (2014), the amplitude of negative superhumps must drastically increase at the brightening as shown in Fig. 1 of Wood and Burke (2007). This expectation is inconsistent with the observational fact that the amplitude of negative superhumps did not change at the brightening phase of the IW And-type light cycle but rather it became a little smaller (see subsection 3.2.3). Furthermore, no enhancement of the orbital hump was observed either at the brightening. These results seem to rule out the enhanced mass transfer model by Hameury and Lasota (2014): the same argument for the disk instability model in the ordinary DN outbursts over the mass-transfer-burst model.

Next, we examine the other model proposed by Kimura et al. (2020), in which the thermal-viscous instability in the tilted disk was studied in the framework of the disk instability model. Some of the observational results seem to be supportive of this model. The observed amplitude variation of negative superhumps (see the third panel of Figure 1) during one cycle of the IW And-type phenomenon seems to be consistent with the assumption that the mass transfer rate stays more or less constant in their model. Moreover, the weak correlation between the tilt angle and the cycle length of the IW And-type phenomenon seems to be consistent with their model, as the cycle interval is longer when the tilt angle is higher (see also subsection 3.4.3). The rapid decrease in the negative-superhump frequency at the brightening phase was also predicted by them (see subsection 4.1).

On the other hand, some other results are not supportive of their model. As discussed in subsection 4.1, the gradual increase in the observational frequency variation of negative superhumps during quasi-standstills cannot be reproduced by their model. Also, it has turned out that the simplified assumption in which the gas stream takes a single-particle trajectory in their model is not realistic to explain the light curve of negative superhumps, as described in subsection 3.2.3. They calculated various mass supply patterns from the secondary under the simplified assumption and reproduced by their numerical simulations a cyclic light curve similar to the IW And-type phenomenon only in the highly-tilted disk model, while the observations suggest a very low tilt angle and the IW And-type phenomenon was observed even when negative superhumps were very weak or disappeared in KIC 9406652 (see subsections 3.2.1 and 3.4.3). Actually, IM Eri, another IW And star, did not show clearly negative superhumps during its IW And-type phenomenon (Kato et al. 2020). We have to modify the calculation

of the mass supply pattern by taking into account the gas-stream overflow and confirm whether the IW And-type phenomenon and the gradual increase of the negative-superhump frequency during quasi-standstills can be reproduced in the non-tilted or slightly-tilted disk. There is a possibility that the most essential condition for the IW And-type phenomenon may be the overflow of the gas stream at the disk rim, reaching the inner part of the disk both in the case of the non-tilted disk and of the tilted disk alike (Hessman 1999; Schreiber and Hessman 1998).

## 5 Summary

We re-investigated the *Kepler* data of KIC 9406652 and performed detailed timing analyses of negative superhumps, orbital signals, and super-orbital modulations. Our main results are summarized as follows.

1. The emergence of negative superhumps was not necessarily correlated with the IW And-type phenomenon (see subsections 3.1 and 3.2.1), which implies that the IW And-type phenomenon may not be directly related to the disk tilt.
2. The frequency of negative superhumps showed cyclic variations corresponding to each cycle of IW And-type phenomena: a rapid decrease during the brightening and a gradual increase during the quasi-standstill (see subsection 3.2.2). This variation would represent the rapid change of the surface density distribution during the brightening and the gradual expansion of the disk during the quasi-standstill (see subsection 4.1). Thus the investigation of frequency variations of negative superhumps will provide an important new tool for understanding the variation of the disk radius and/or the radial mass distribution in a tilted accretion disk.
3. The amplitudes of the negative superhumps did not vary with time so much in the flux scale, even though the intrinsic disk luminosity varies greatly during one cycle of the IW And-type phenomenon (see subsection 3.2.3). This suggests that negative superhumps are caused by the variable dissipation of the bright spot as the gas stream sweeps the tilted disk surface with the negative superhump cycle.
4. The light curve of the negative superhumps was single-peaked and it showed a great variety (see subsection 3.2.3). This implies that a part of the gas stream always overflows the disk edge and other parts collide with the disk edge in the slightly tilted disk.
5. The orbital signal consists of the three components: the irradiation of the secondary by the tilted disk and the WD, the orbital hump formed at the disk rim by the gas stream, and the ellipsoidal modulation (see subsection 3.3). The irradiation effect was dominant when the disk became bright, while the orbital hump dominated when the system was in the dip and/or when the tilt angle of the disk was almost non-tilted. The contribution of the ellipsoidal modulation is very small, only a few percent to the total orbital signal.
6. The frequency variation of super-orbital modulation was consistent with that of negative superhumps, which means that both of the phenomena have the same origin: the tilted disk (see subsection 3.4.1).
7. The tilt angle was estimated to be less than 3 deg from the time variation of the semi-amplitude of super-orbital modulations, which are consistent with the amplitude and profile variations of negative superhumps (see subsection 3.4.3).
8. The orbital light curve, particularly in the brightening stage, varied greatly with the phase of super-orbital modulation, i.e., with the orientation of the tilted disk to the observer (see subsection 3.5). Its amplitude was the largest at the minimum of super-orbital modulations and the smallest at the opposite phase. The light maximum of the orbital light curve shifted to an earlier phase as the phase of the super-orbital modulation advances. These phenomena are understood as the upper face of the secondary star is irradiated by the tilted disk: clear evidence that the disk was tilted out of the orbital plane of the binary system and it precessed ‘retrogradely’.
9. We have evaluated the recently proposed two models for IW And stars by the results of our analyses (see subsection 4.2). Any supportive results have not been obtained for the model proposed by Hameury and Lasota (2014). On the other hand, a part of the frequency variation of negative superhumps does not support the model proposed by Kimura et al. (2020), while some of our results: the amplitude variation of negative superhumps and the correlation between the tilt angle and the cycle length of the IW And-type phenomenon seem to support this model. There might be a possibility that the extension of this model can reproduce the IW And-type phenomenon better if we take into account the gas-stream overflow.

## Acknowledgements

This work was financially supported by the Grant-in-Aid for JSPS Fellows for young researchers (M. Kimura). M. Kimura acknowledges support by the Special Postdoctoral Researchers Program at RIKEN. The numerical code that we used in this paper is provided by Izumi Hachisu. We thank the anonymous referee for helpful comments.

## Supporting information

Additional supporting information can be found in the online version of this article: supplementary tables E1–E8 and supplementary figures E1–E28.



## References

- Armitage, P. J., & Livio, M. 1998, *ApJ*, 493, 898
- Armstrong, E., et al. 2013, *MNRAS*, 435, 707
- Bonnet-Bidaud, J. M., Motch, C., & Mouchet, M. 1985, *A&A*, 143, 313
- Cleveland, W. S. 1979, *J. Amer. Statist. Assoc.*, 74, 829
- Fernie, J. D. 1989, *PASP*, 101, 225
- Gies, D. R., et al. 2013, *ApJ*, 775, 64
- Hachisu, I., & Kato, M. 2001, *ApJ*, 558, 323
- Hameury, J.-M., & Lasota, J.-P. 2014, *A&A*, 569, A48
- Hessman, F. V. 1999, *ApJ*, 510, 867
- Honeycutt, R. K. 2001, *PASP*, 113, 473
- Ichikawa, S., & Osaki, Y. 1992, *PASJ*, 44, 15
- Kato, T. 2019, *PASJ*, 71, 20
- Kato, T., et al. 2009, *PASJ*, 61, S395
- Kato, T., et al. 2010, *PASJ*, 62, 1525
- Kato, Taichi, et al. 2019, *PASJ*, 71, L1
- Kato, Taichi, et al. 2020, *PASJ*, 72, 11
- Kimura, Mariko, Osaki, Yoji, Kato, Taichi, & Mineshige, Shin 2020, *PASJ*, 72, 22
- Krzeminski, W. 1965, *ApJ*, 142, 1051
- Kunze, S., Speith, R., & Hessman, F. V. 2001, *MNRAS*, 322, 499
- Larwood, J. 1998, *MNRAS*, 299, L32
- Lubow, S. H., & Shu, F. H. 1975, *ApJ*, 198, 383
- Murphy, Simon J. 2012, *MNRAS*, 422, 665
- Murray, J. R., Chakrabarty, D., Wynn, G. A., & Kramer, L. 2002, *MNRAS*, 335, 247
- Osaki, Y. 1989, *PASJ*, 41, 1005
- Osaki, Y. 1996, *PASP*, 108, 39
- Osaki, Y., & Kato, T. 2013, *PASJ*, 65, 95
- Osaki, Y., & Kato, T. 2014, *PASJ*, 66, 15
- Papaloizou, John C. B., & Terquem, Caroline 1995, *MNRAS*, 274, 987
- Patterson, J. 1999, in *Disk Instabilities in Close Binary Systems*, ed. S. Mineshige, & J. C. Wheeler (Tokyo: Universal Academy Press), p. 61
- Schreiber, M. R., & Hessman, F. V. 1998, *MNRAS*, 301, 626
- Simonsen, M. 2011, *J. American Assoc. Variable Star Obs.*, 39, 66
- Simonsen, M., Bohlson, T., Hamsch, F.-J., & Stubbings, R. 2014, *J. American Assoc. Variable Star Obs.*, 42, 199
- Smak, J. 1992, *Acta Astron.*, 42, 323
- Smak, J. 2009, *Acta Astron.*, 59, 419
- Stellingwerf, R. F. 1978, *ApJ*, 224, 953
- Szkody, P., et al. 2013, *PASP*, 125, 1421
- Warner, B. 1995, *Cataclysmic Variable Stars* (Cambridge: Cambridge University Press)
- Wood, M. A., & Burke, C. J. 2007, *ApJ*, 661, 1042
- Wood, M. A., Montgomery, M. M., & Simpson, J. C. 2000, *ApJ*, 535, L39